
Article:
Yang, W. orcid.org/0000-0002-8045-3901, Chen, J. orcid.org/0000-0001-8341-1849, Liu, W. et al. (2 more authors) (2017) A Modified Three-Step Algorithm for TOPS and Sliding Spotlight SAR Data Processing. IEEE Transactions on Geoscience and Remote Sensing, 55 (12). pp. 6910-6921. ISSN 0196-2892

https://doi.org/10.1109/TGRS.2017.2735993

A Modified Three-Step Algorithm for TOPS and Sliding Spotlight SAR Data Processing

Wei Yang, *Member, IEEE*, Jie Chen, *Member, IEEE*, Wei Liu, *Senior Member, IEEE*, Pengbo Wang, *Member, IEEE* and Chunsheng Li

***Abstract*—There are two challenges for efficient processing of both the sliding spotlight and Terrain Observation by Progressive Scans (TOPS) data using full-aperture algorithms. First, to overcome Doppler spectrum aliasing, zero padding is required for azimuth up-sampling, increasing the computation burden; second, the azimuth deramp operation for avoiding SAR image folding leads to azimuth time shift along the range dimension, and in turn the appearance of ghost targets and azimuth resolution reduction at the scene edge, especially in the wide-swath case. In this paper, a novel three-step algorithm is proposed for processing the sliding spotlight and TOPS data. In the first step, a modified de-rotation is derived in detail based on the chirp-z transform, avoiding zero-padding; then, the chirp scaling algorithm kernel is adopted for precise focusing in the second step; in the third step, instead of the traditional range-independent deramp, a range-dependent deramp is applied to compensate for the time shift. Moreover, the SAR image geometry distortion caused by range-dependent deramp is corrected by employing a range-dependent chirp-z transform. Experimental results based on both simulated data and real data are provided to validate the proposed algorithm.**

***Index Terms*—Synthetic aperture radar (SAR), Terrain Observation by Progressive Scans (TOPS), Sliding Spotlight, Chirp-Z**

I. Introduction

By steering the azimuth antenna beam either mechanically or electronically, several advanced imaging modes, including TOPS and sliding spotlight [1]-[5], have been proposed for achieving a higher resolution or wider swath coverage, to meet the rising application demands in monitoring, interferometry, classification, and tomography [6]-[10]. For example, TOPS and sliding spotlight imaging modes have been adopted in current state-of-the-art satellites TerraSAR-X, TanDEM-X, and Sentinel-1 [11]-[13], as well as the next generation SAR satellites such as TerraSAR NEXT GENERATION (TerraSAR-NG) [14], [15].

Due to azimuth antenna beam steering, a common feature of the sliding spotlight and the TOPS imaging modes is a linear variation of Doppler centroid in azimuth. Consequently, the total azimuth signal bandwidth may span over several pulse repetition frequency (PRF) intervals, resulting in Doppler spectrum aliasing. To overcome this problem, the spectrum mosaicking method was proposed in [1], [16]-[17], but it is inefficient due to the complex spectrum copying, mosaicking, filtering and resampling operations [18]. Therefore, advanced sub-aperture and full-aperture processing methods were provided for TOPS and sliding spotlight data processing without spectrum mosaicking. For sub-aperture based methods [19], sub-aperture formation is performed by taking advantage of the higher PRF with respect to the instantaneous azimuth bandwidth. The extended chirp scaling algorithm (ECSA) was employed for TerraSAR-X TOPS data processing firstly in [20], and then based on the ECSA, the baseband azimuth scaling algorithm (BASA) was proposed for TOPS and sliding spotlight data processing, with its performance verified by TerraSAR-X data [21]. Since additional sub-aperture formation and sub-aperture recombination operations are required in sub-aperture processing algorithms, the introduced small blocks will affect the processing efficiency. Therefore, to avoid the sub-aperture formation and recombination operations, full-aperture algorithms were proposed, which employ the de-rotation operation to compensate for the extra Doppler bandwidth caused by antenna steering [22]-[25]. However, zero padding in azimuth is needed to avoid Doppler spectrum aliasing after the de-rotation operation, which increases the computational burden, especially in the sliding spotlight case [4], [22], [26]. A moving band chirp Z-transform (MBCZT) was proposed for eliminating the effect of zero-padding in TOPS data processing [27], [28]. However, the MBCZT is implemented by fast Fourier transform (FFT) and complex multiplications, and time aliasing is still a problem during the operation, which is not considered in the MBCZT.

In addition, azimuth folding in the focused image is another challenge in TOPS and sliding spotlight data processing. The deramp operation is an efficient method to circumvent azimuth folding [21],[23], but it will lead to azimuth time-shift along the range dimension [29]. In the wide coverage case, the time-shift will cause the wrapping effect in azimuth at the scene edge, resulting in appearance of ghost targets and reduction in azimuth resolution. As a result, data division in range is required to accommodate the time-shift, which introduces the extra azimuth resampling and range sub-image combination operations.

In this paper, a modified three-step algorithm is proposed for

W. Yang, J. Chen and P. Wang are with the School of Electronic and Information Engineering, Beihang University, Beijing 100191, China. (e-mail: chenjie@buaa.edu.cn)

W. Liu is with the Department of Electronic and Electrical Engineering, University of Sheffield, Sheffield S1 3JD, U.K.

sliding spotlight and TOPS data processing without sub-aperture formation. The modified de-rotation is derived in detail based on the chirp-z transform (CZT), and the selection of CZT scaling factor is analyzed as well, which avoids the zero-padding operation. After focusing using the chirp scaling algorithm (CSA) kernel, the range-dependent deramp method is employed to accommodate the azimuth time-shift, instead of the traditional range-independent deramp. However, the range-dependent deramp will lead to azimuth sampling variation along the range dimension, causing image geometry distortion. To correct the distortion, range-dependent CZT is implemented, providing the same azimuth pixel sampling interval for all range bins. By the modified three-step algorithm, the sliding spotlight and TOPS data can be processed efficiently, without sub-aperture formation in azimuth and data division in range.

This paper is organized as follows. The two considered imaging modes are reviewed in Section II. In Section III, the proposed modified three-step algorithm is derived in detail, as well as a discussion of the involved scaling factor. Simulation results are provided in Section IV, and conclusions are drawn in Section V.

II. IMAGING MODES

The antenna steering technique is employed in both the TOPS and sliding spotlight modes. As shown in Fig. 1, T_B is the illumination time of the whole scene, v_e is the effective velocity, ω_φ is the rotation rate, r is the minimum distance from the SAR sensor to the ground, A is the point target located at (x_a, r), X_s corresponds to the valid area with full illumination time, and X_f corresponds to the area with insufficient illumination time. In order to distinguish the difference of the TOPS and the sliding spotlight modes in the following discussion, we introduce the rotation range distance r_{rot}, which represents the minimum distance from the virtual rotation point (VRP) to the SAR sensor. By defining upward direction as positive, r_{rot} is negative in TOPS mode and positive in sliding spotlight mode.

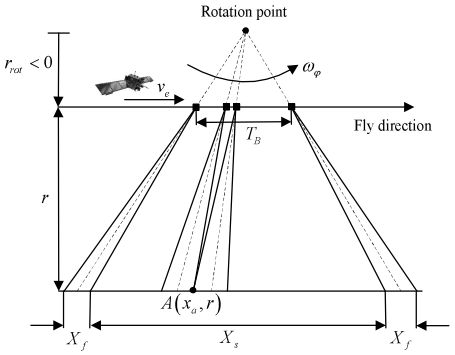

(a)

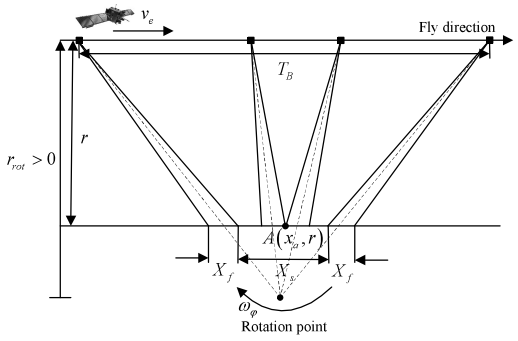

(b)

Fig. 1 Acquisition geometry of the two modes: (a) TOPS, (b) sliding spotlight.

A. The TOPS Mode

In conventional ScanSAR mode, targets located at different azimuth positions are illuminated by different parts of the azimuth antenna pattern (AAP), resulting in problems of scalloping, and azimuth-varying distributed target ambiguity ratio and signal-to-noise ratio (SNR) [30], [31]. To overcome these problems, antenna steering is performed in the TOPS mode, leading to complete AAP weighting for all the targets located in X_s. Consequently, the scalloping, azimuth-varying ambiguity and SNR are eliminated.

In TOPS mode, a very long burst is obtained, at the cost of shorter target illumination time. Therefore, the Doppler bandwidth of each target B_t is smaller than the pulse repetition frequency (PRF), referred to as f_{prf}. However, the total Doppler bandwidth B_{total} may span over several PRF intervals due to the extra bandwidth B_{steer}, caused by antenna steering, as shown by the time-frequency diagram (TFD) in Fig. 2(a). Therefore, if azimuth FFT is applied directly to raw data, Doppler spectrum aliasing will occur in the TOPS mode.

B. The Sliding Spotlight Mode

Compared with the TOPS mode, the sliding spotlight mode performs a clockwise steering with the VRP located underground. By doing that, on the one hand, a longer target illumination time is obtained compared with the strip-map mode, which results in a high azimuth resolution. On the other hand, compared with the spotlight mode, the target illumination time becomes shorter, but the azimuth swath is enlarged. Therefore, the sliding spotlight mode is a compromise between the spotlight and strip-map mode. However, by increasing the azimuth steering angle, the requirements of azimuth resolution and swath can be satisfied at the same time, a clear advantage over both the strip-map and spotlight modes.

Since a high azimuth resolution is obtained in the sliding spotlight mode, the target Doppler bandwidth is larger than PRF, and similar to TOPS, the total Doppler bandwidth also spans over several PRF intervals, as shown in Fig. 2(b). As a result, the same Doppler spectrum aliasing problem exists and should be solved in processing both the TOPS and sliding spotlight data.

C. Signal Model

For both operating modes, a unified signal model can be expressed as follows [23]

$$\begin{aligned} S(\tau,\eta;x_a,r) &= rect\left[\frac{\eta}{T_B}\right]\cdot rect\left[\frac{x_a}{X_s}\right] \\ &\cdot rect\left[\frac{v_e\eta/\gamma(r)-x_a}{X_f}\right]\cdot rect\left[\tau-\frac{2R(\eta;x_a,r)}{c}\right] \\ &\cdot\exp\left\{-j\pi b\left(\tau-\frac{2R(\eta;x_a,r)}{c}\right)^2\right\} \\ &\cdot\exp\left\{-j\frac{4\pi R(\eta;x_a,r)}{\lambda}\right\} \end{aligned} \tag{1}$$

where $rect[\cdot]$ represents the rectangular envelope, b is the signal frequency modulation rate, c is the speed of light, λ is the wavelength, τ is the range time, η is the azimuth, and $R(\eta;x_a,r)$ is the instantaneous distance between the sensor and the target point $A(x_a,r)$. With $x_a=v_e\eta_a$, $R(\eta;x_a,r)$ is given by

$$R(\eta;\eta_a,r)=\sqrt{r^2+v_e^2(\eta-\eta_a)^2} \tag{2}$$

And $\gamma(r)$ is a hybrid factor, which is range-dependent, defined as follows:

$$\gamma(r)=\frac{r_{rot}}{r_{rot}-r} \tag{3}$$

In the TOPS mode, r_{rot} is negative, whereas r_{rot} is positive in the sliding spotlight mode. Therefore,

$$\gamma(r)=\begin{cases}0\sim 1 & \text{TOPS}\\ 1\sim+\infty & \text{Sliding spotlight}\end{cases} \tag{4}$$

Performing the azimuth FFT, we obtain the target Doppler bandwidth B_t and the total Doppler bandwidth B_{total} given by (5) and (6) [23].

$$B_t = B_{\Delta\theta}\cdot\gamma(r) \tag{5}$$

$$B_{total}=B_{\Delta\theta}+B_{steer}=B_{\Delta\theta}+K_{rotation}\cdot T_B \tag{6}$$

where $B_{\Delta\theta}=2v_e/D$ is the instantaneous bandwidth, D is the antenna length, and $k_{rotation}$ is the de-rotation chirp rate, given by

$$k_{rotation}=\frac{2v_e^2}{\lambda r_{rot}} \tag{7}$$

Note that B_t is range-dependent, which means the azimuth resolution varies in the range dimension. However, B_{total} is range-independent, consisting of $B_{\Delta\theta}$ and B_{steer}.

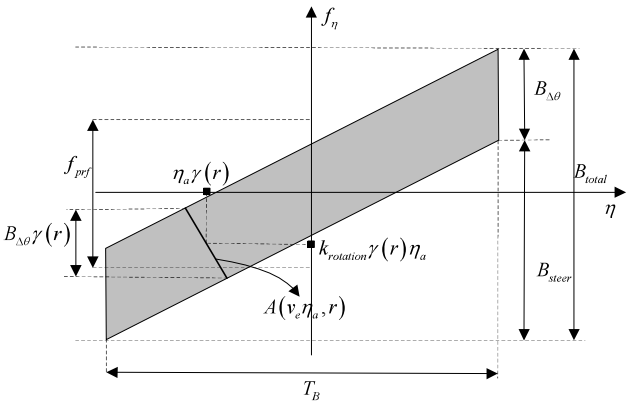

(a)

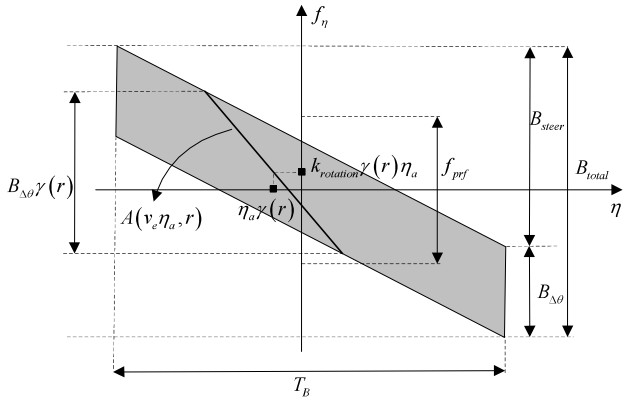

(b)

Fig. 2 TFDs of the two modes. The illuminated center time of target point $A(x_a,r)$ is $\eta_a\gamma(r)$, and the Doppler centroid frequency is $k_{rotation}\gamma(r)\eta_a$. (a) TOPS (b) Sliding spotlight.

III. The Modified Three-Step Algorithm

Since the current imaging algorithm kernels have a good performance for range compression and range cell migration correction (RCMC) [16], [19], [32-35], the contribution of this paper is mainly focused on azimuth processing, which can be implemented without zero padding and sub-aperture formation in azimuth.

A. Properties after de-rotation

In order to overcome spectrum aliasing, several methods have been proposed, including frequency mosaic [1], sub-aperture processing [21], and the de-rotation processing [23], [36], [37]. Among them the de-rotation operation is the most efficient [25]. Therefore, a range-independent de-rotation method is adopted in this paper.

For simplicity and without loss of generality, the azimuth signal can be expressed as follows

$$\begin{aligned} S(\eta;\eta_a,r) &= rect\left[\frac{v_e\eta/\gamma(r)-x_a}{X_f}\right]\cdot rect\left[\frac{\eta}{T_{total}}\right]\cdot rect\left[\frac{x_a}{X_s}\right] \\ &\cdot\exp\left\{-j\frac{4\pi R(\eta;x_a,r)}{\lambda}\right\} \end{aligned} \tag{8}$$

The de-rotation operation involves azimuth signal

convolution between the azimuth signal and a selected chirp signal, given by

$$H_{de-ro}(\eta)=\exp\left\{j\pi k_{rotation}\eta^2\right\} \tag{9}$$

The convolution result is [35]

$$\begin{aligned} S'_{A,\eta}(\eta;\eta_a,r) &= S_{A,\eta}(\eta;\eta_a,r)\otimes_* H_{de-ro}(\eta) \\ &= rect\left[-\frac{\eta}{\lambda r_{rot}/(Dv_e)}\right]\cdot rect\left[\frac{\eta-\eta_a r_{rot}/r}{T_B(r-r_{rot})/r}\right] \\ &\cdot rect\left[\frac{\eta_a}{X_s/v_e}\right]\cdot\exp\left\{j\pi k_e(r)(\eta-\eta_a)^2\right\} \end{aligned} \tag{10}$$

where $\otimes_*$ indicates the convolution operation, and

$$k_e(r)=\frac{2v_e^2}{\lambda(r_{rot}-r)} \tag{11}$$

Now we discuss the azimuth signal properties after de-rotation. According to (10), the value range of the azimuth signal is determined by three terms. The first term limits the value of η, referred to as η_1,

$$\eta_1\in\left(-\frac{\lambda|r_{rot}|}{2Dv_e},\frac{\lambda|r_{rot}|}{2Dv_e}\right) \tag{12}$$

Note that the second term η_2 is a function of η_a, which varies with η_a,

$$\eta_2\in\left(-\frac{T_B|(r-r_{rot})|}{2r}+\frac{\eta_a r_{rot}}{r},\frac{T_B|(r-r_{rot})|}{2r}+\frac{\eta_a r_{rot}}{r}\right) \tag{13}$$

With respect to η_a, it is determined by the third term

$$\eta_a\in\left(-\frac{X_s}{2v_e},\frac{X_s}{2v_e}\right) \tag{14}$$

Substituting the maximum and the minimum values of η_a to (13), the boundary values of η_2 that correspond to targets located at the azimuth edge can be calculated by

$$\eta_2\big|_{\eta_a=X_s/(2v_e)}\in\left(-\frac{T_B|r-r_{rot}|}{2r}+\frac{X_s r_{rot}}{2v_e r},\frac{T_B|r-r_{rot}|}{2r}+\frac{X_s r_{rot}}{2v_e r}\right) \tag{15}$$

$$\eta_2\big|_{\eta_a=-X_s/(2v_e)}\in\left(-\frac{T_B|r-r_{rot}|}{2r}-\frac{X_s r_{rot}}{2v_e r},\frac{T_B|r-r_{rot}|}{2r}-\frac{X_s r_{rot}}{2v_e r}\right) \tag{16}$$

Then, we compare the boundary values of η_1 and η_2. Taking the TOPS mode as an example and comparing (12) and (15), the boundary value difference is calculated with $\eta_a=X_s/(2v_e)$

$$\begin{aligned} \Delta\eta_d\big|^{\max}_{\eta_a=X_s/(2v_e)} &= \frac{\lambda|r_{rot}|}{2Dv_e}-\left(\frac{T_B|r-r_{rot}|}{2r}+\frac{X_s}{2v_e}\frac{r_{rot}}{r}\right) \\ &= -\frac{\lambda r_{rot}}{2Dv_e}-\frac{X_s}{2v_e}\frac{r_{rot}}{r}-\frac{T_B(r-r_{rot})}{2r} \\ &= -\frac{X_f}{2v_e}\frac{r_{rot}}{r}-\frac{X_s}{2v_e}\frac{r_{rot}}{r}-\frac{T_B(r-r_{rot})}{2r}=0 \end{aligned} \tag{17}$$

$$\begin{aligned} \Delta\eta_d\big|^{\min}_{\eta_a=X_s/(2v_e)} &= -\frac{\lambda|r_{rot}|}{2Dv_e}-\left(-\frac{T_B|r-r_{rot}|}{2r}+\frac{X_s}{2v_e}\frac{r_{rot}}{r}\right) \\ &= \left(\frac{\lambda r_{rot}}{2Dv_e}+\frac{X_s}{2v_e}\frac{r_{rot}}{r}+\frac{T_B(r-r_{rot})}{2r}\right)-\frac{X_s}{v_e}\frac{r_{rot}}{r} \\ &= -\frac{X_s}{v_e}\frac{r_{rot}}{r}>0 \end{aligned} \tag{18}$$

Comparing (12) and (16), we can calculate the boundary value difference with $\eta_a=-X_s/(2v_e)$

$$\Delta\eta_d\big|^{\max}_{\eta_a=-X_s/(2v_e)}=\frac{\lambda|r_{rot}|}{2Dv_e}-\left(\frac{T_B|r-r_{rot}|}{2r}-\frac{X_s r_{rot}}{2v_e r}\right)=\frac{X_s}{v_e}\frac{r_{rot}}{r}<0 \tag{19}$$

$$\Delta\eta_d\big|^{\min}_{\eta_a=-X_s/(2v_e)}=-\frac{\lambda|r_{rot}|}{2Dv_e}-\left(-\frac{T_B|r-r_{rot}|}{2r}-\frac{X_s}{2v_e}\frac{r_{rot}}{r}\right)=0 \tag{20}$$

According to equations from (17) to (20), the relationship of η_1 and η_2 is given by

$$\eta_1\in\eta_2 \tag{21}$$

The value ranges of η_1 and η_2 are shown in Fig. 3.

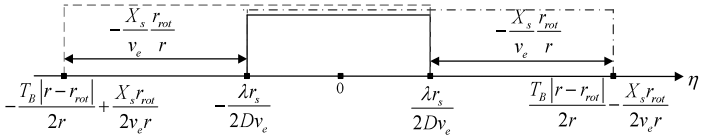

Fig. 3 The value range of azimuth signal after a de-rotation operation corresponding to the targets located at the area with full illumination time. Black solid, red dashed and blue dash-dot rectangular windows represent the value range of η_1, $\eta_2\big|_{\eta_a=X_s/(2v_e)}$, and $\eta_2\big|_{\eta_a=-X_s/(2v_e)}$ respectively.

All the above analysis only considers the targets located at X_s with full illumination time. Next, we further give a short discussion about the targets located at X_f, which are illuminated with insufficient time. According to Fig. 1, the value range of η_a corresponding to the area X_f is given by

$$\eta_a\in\left(-\frac{X_s}{2v_e}-\frac{X_f}{v_e},-\frac{X_s}{2v_e}\right)\cup\left(\frac{X_s}{2v_e},\frac{X_s}{2v_e}+\frac{X_f}{v_e}\right) \tag{22}$$

Using the same method, we can calculate the boundary value difference as follows:

$$\Delta\eta_d\big|^{\max}_{\eta_a=X_s/(2v_e)+X_f/v_e}=-\frac{X_f}{v_e}\frac{r_{rot}}{r}=\frac{\lambda|r_{rot}|}{Dv_e}>0 \tag{23}$$

$$\Delta\eta_d\big|^{\min}_{\eta_a=-X_s/(2v_e)+X_f/v_e}=-\frac{X_s+X_f}{v_e}\frac{r_{rot}}{r}>0 \tag{24}$$

$$\Delta\eta_d\big|^{\max}_{\eta_a=-X_s/(2v_e)-X_f/v_e}=\frac{X_s+X_f}{v_e}\frac{r_{rot}}{r}<0 \tag{25}$$

$$\Delta\eta_d\big|^{\min}_{\eta_a=-X_s/(2v_e)-X_f/v_e}=\frac{X_f}{v_e}\frac{r_{rot}}{r}=-\frac{\lambda|r_{rot}|}{Dv_e}<0 \tag{26}$$

Based on (23) to (26), after the de-rotation operation, the value range of the azimuth signal is determined by the overlapped value range of η_1 and η_2. The value range of η_2 with $\eta_a=X_s/(2v_e)-X_f/v_e$ and $\eta_a=X_s/(2v_e)-X_f/v_e$ are

shown in Fig. 4, with red dashed and blue dash-dot rectangular windows, respectively.

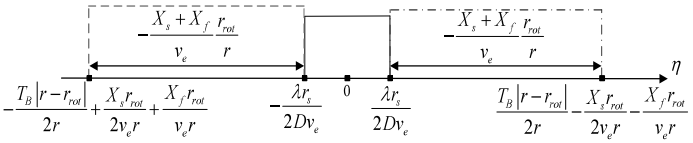

Fig. 4 The value range of azimuth signal after a de-rotation operation corresponding to the targets located at the area with insufficient illumination time. Black solid, red dashed and blue dashdot rectangular windows represent the value range of η_1, $\eta_2|_{\eta_a=X_s/(2v_e)+X_f/v_e}$, and $\eta_2|_{\eta_a=-X_s/(2v_e)-X_f/v_e}$, respectively.

Whether the targets have full illumination time or not, the value range of azimuth signal after de-rotation falls into $\left[-\left(\lambda|r_{rot}|\right)/\left(2Dv_e\right),\left(\lambda|r_{rot}|\right)/\left(2Dv_e\right)\right]$. Therefore, the first term of (10) plays the dominant role, allowing us to simplify (10) as follows:

$$S'_{A,\eta}\left(\eta;\eta_a,r\right)=rect\left[-\frac{\eta}{\lambda r_{rot}/\left(Dv_e\right)}\right]\cdot\exp\left\{j\pi k_e\left(r\right)\left(\eta-\eta_a\right)^2\right\} \quad (27)$$

Note that the same conclusion can be drawn in the case of sliding spotlight mode.

B. Modified de-rotation based on CZT

After de-rotation, the equivalent sampling rate $f_{prf}^{(1)}$ in azimuth can be expressed as [35]:

$$f_{prf}^{(1)}=\frac{N_a k_{rotation}}{f_{prf}} \quad (28)$$

To avoid Doppler spectrum aliasing, $f_{prf}^{(1)}$ should be larger than B_{total}, i.e.,

$$f_{prf}^{(1)}=\frac{N_F k_{rotation}}{f_{prf}}>B_{total}=B_{\Delta\theta}+B_{steer} \quad (29)$$

So, we further rewrite (29) as

$$N_F>\frac{B_{\Delta\theta}f_{prf}}{k_{rotation}}+\frac{B_{steer}}{k_{rotation}}f_{prf}=\frac{B_{\Delta\theta}f_{prf}}{k_{rotation}}+N_A \quad (30)$$

where N_F is the number of FFT points, and N_A is the azimuth point number of raw data. Therefore, zero-padding is needed to avoid spectrum aliasing, and the point number for zero-padding is determined by $B_{\Delta\theta}f_{prf}/k_{rotation}$, which is range-independent. Moreover, in practice, radix-2 FFT is usually adopted, which means that if the point number after zero-padding is larger than the point number of radix-2 FFT, in order to perform the radix-2 FFT, the point number will be more than twice the azimuth point number of the raw data. Consequently, more memory is required, and the computational burden increases, affecting the processing efficiency.

In existing processing algorithms, instead of performing convolution directly, the de-rotation is usually realized by FFT and complex multiplications, including azimuth dechirp, azimuth FFT, and azimuth rechirp, as shown in Fig. 5(a). To mitigate the effects due to zero-padding, a modified de-rotation approach is presented based on CZT [36-38], which is implemented by CZT instead of azimuth FFT, as shown in Fig. 5(b).

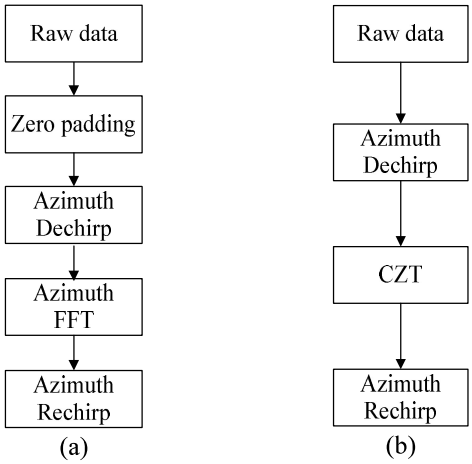

Fig. 5 Implementation of the de-rotation operation: (a) traditional approach, (b) proposed approach.

The azimuth dechirp operation is performed by multiplying the azimuth signal with (9), which compensates the Doppler bandwidth caused by antenna steering. Then, the CZT is employed with the selected spectrum sampling interval $\Delta f_{\eta,1}$, given by

$$\Delta f_{\eta,1}=\alpha\frac{f_{prf}}{N_A} \quad (31)$$

where α is the scaling factor. Subsequently, azimuth rechirp is implemented to complete the de-rotation operation.

Since the CZT is adopted, the equivalent sampling rate can be rewritten as

$$f_{prf}^{(1)}=\frac{k_{rotation}}{\Delta f_{\eta,1}}=\frac{k_{rotation}}{\alpha}\frac{N_A}{f_{prf}} \quad (32)$$

On the one hand, to avoid Doppler spectrum aliasing, substituting (32) to (29), we can obtain the upper limit of α,

$$\alpha_{upper}<\frac{T_B}{T_B+T_1} \quad (33)$$

where T_1 is the time domain width of the azimuth signal after de-rotation, given by

$$T_1=\frac{\lambda|r_{rot}|}{Dv_e} \quad (34)$$

On the other hand, to avoid azimuth time aliasing after the de-rotation operation, the time domain width of the output signal, denoted by T_{DE}, should be larger than T_1,

$$T_{DE}=\frac{N_A}{f_{prf}^{(1)}}=\alpha\frac{f_{prf}}{k_{rotation}}>\frac{\lambda|r_{rot}|}{Dv_e} \quad (35)$$

Then, combining (34) and (35), we can calculate the lower limit of α,

$$\alpha_{lower}>\frac{B_{\Delta\theta}}{f_{prf}} \quad (36)$$

Moreover, as shown in Fig. 6, the chirp-z transform in the discrete domain is given by [36]

$$I[m] = CZT\left(S'_{A,\eta}[n]\right) = W^{\frac{m^2}{2}} \cdot \left[\left(S'_{A,\eta}[n]\cdot Q^{-n}\cdot W^{\frac{n^2}{2}}\right) \otimes_* W^{-\frac{n^2}{2}}\right] \quad (37)$$

where $m, n \in [0, N_A - 1]$, and $I[m]$ is the output result. Furthermore, the convolution operation in (37) is realized by FFT and complex multiplications as follows:

$$I[m] = W^{\frac{m^2}{2}} \cdot IFFT\left[FFT\left(S'_{A,\eta}[n]\cdot Q^{-n}\cdot W^{\frac{n^2}{2}}\right)\cdot FFT\left(W^{-\frac{n^2}{2}}\right)\right] \quad (38)$$

where Q and W are given by (39) and (40), respectively.

$$Q = \exp\left\{-j\frac{\pi N_A \Delta f_{\eta,1}}{f_{prf}}\right\} \quad (39)$$

$$W = \exp\left\{-j\frac{2\pi \Delta f_{\eta,1}}{f_{prf}}\right\} \quad (40)$$

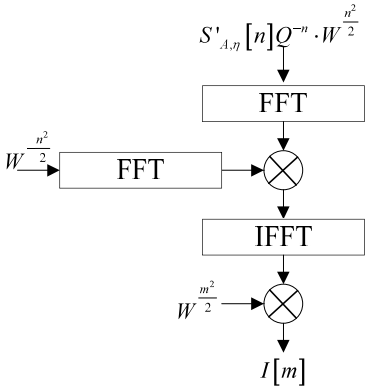

Fig. 6 The detailed implementation of CZT.

In order to verify the advantages of the proposed approach, taking sliding spotlight mode as an example, we perform a simple simulation using the parameters listed in Table I, Section IV. Fig. 7 shows the comparison results in the range-Doppler domain. Without zero-padding, Doppler spectrum aliasing occurs using the traditional approach, whereas by the proposed one with $\alpha = 0.8$, the Doppler spectrum aliasing has been removed.

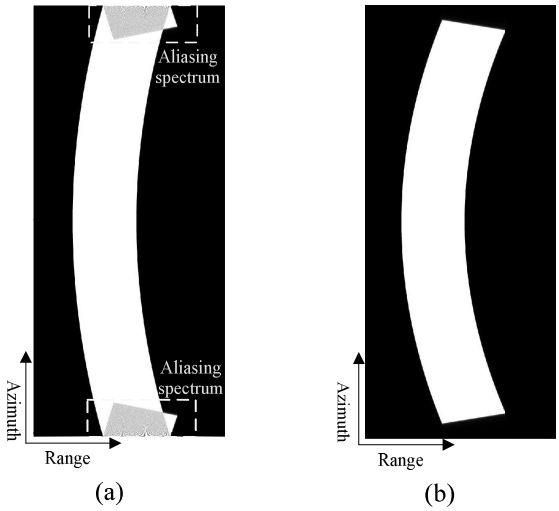

Fig. 7 Comparison of the de-rotation results: (a) traditional approach without zero-padding, (b) proposed approach with $\alpha = 0.8$.

In fact, the proposed approach takes advantage of the higher PRF with respect to the instantaneous azimuth bandwidth, which can be used for improving the azimuth sampling rate with an appropriate α. However, the value range is still limited by (33) and (36). On the one hand, if α is larger than α_{upper}, Doppler spectrum aliasing cannot be removed completely; on the other hand, if α is smaller than α_{lower}, there will be azimuth spectrum loss. Using the same parameters as in Fig. 7, we implemented the proposed approach with $\alpha = 0.95$ and $\alpha = 0.4$, which are larger than α_{upper} and smaller than α_{lower}, respectively. As shown in Fig. 8(a), compared with the traditional approach, although the equivalent sampling rate is improved with $\alpha = 0.95$, it is smaller than the Doppler bandwidth. Therefore, Doppler spectrum aliasing still occurs. Moreover, if $\alpha = 0.4$, the equivalent sampling rate is large enough for avoiding Doppler spectrum aliasing. However, since α is smaller than α_{lower}, which means $T_1 > T_{DE}$. Therefore, part of the signal will be lost, resulting in Doppler spectrum loss, as shown in Fig. 8(b). Consequently, azimuth resolution will suffer from significant degradation due to partial loss of the Doppler spectrum.

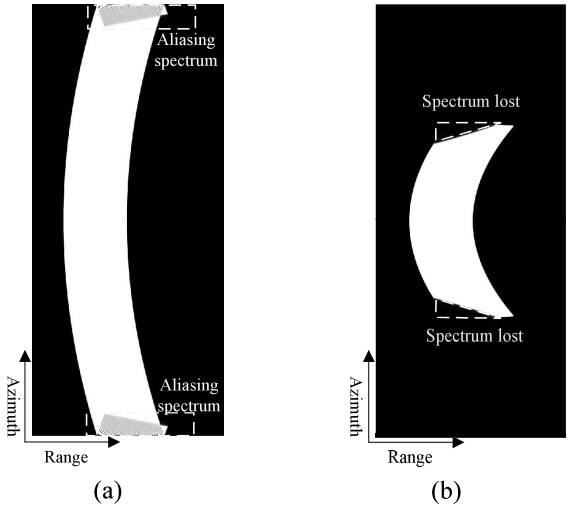

Fig. 8 De-rotation results: (a) proposed approach with $\alpha = 0.95$, (b) proposed approach with $\alpha = 0.4$.

Note that in the case of super-high resolution, the extra residual azimuth bandwidth caused by the bandwidth of linear frequency modulated (LFM) signal should be taken into account [25], [41], which means that α_{lower} will become larger. Moreover, the proposed approach can also be adopted in the squint case, in combination with linear range walk correction (LRWC) [34], [42], [43].

C. Focusing

Many algorithms have been proposed for sliding spotlight and TOPS data processing. Since sliding spotlight is a high-resolution imaging mode, CSA based algorithms are usually adopted for data focusing [21], [25], [34]. With the resolution improved further, WDA and hybrid correlation based

algorithms are employed [26], [41], which are more accurate than CSA based algorithms but less efficient. Moreover, in [44], several important aspects that need to be considered are analyzed, including stop-and-go approximation, curved orbit, and atmospheric effects, with the corresponding compensation methods provided.

Compared with sliding spotlight mode, the TOPS mode is a wide-swath imaging mode with low/moderate resolution, easier for accurate focusing. The WDA kernel was first adopted for TOPS data processing in [1]. However, the WDA kernel cannot accommodate the effective velocity variation along the slant range, and as a result it is not suitable for wide-swath TOPS data processing. Therefore, CSA kernel is usually used for TOPS data precise focusing with a high efficiency [18], [20]-[21], [22]-[24]. In addition, in order to avoid the additional resampling operation during sub-swath image mosaic, both range and azimuth scaling methods can be utilized to provide the sample pixel interval in both azimuth and range for all the sub-swath images [29]. Moreover, some techniques for the enhanced processing of TOPSAR data were introduced in [45], which were demonstrated using the Sentinel-1 TOPS data.

D. Range-dependent deramp operation combined with CZT

To avoid azimuth folding in the focused image, the range-independent deramp operation can be performed by multiplying a constant linear frequency modulation function for the whole sub-swath, given by:

$$H_1\left(f_\eta;r_{ref}\right)=\exp\left\{j\pi\frac{f_\eta^2}{k_{rotation}}\right\}\cdot\exp\left\{-j\pi\frac{f_\eta^2}{k_e\left(r_{ref}\right)}\right\} \tag{41}$$

where r_{ref} is the reference range (we usually choose mid- range as the reference range), and $k_e\left(r_{ref}\right)$ is given by (11) with $r=r_{ref}$.

After azimuth scaling with $H_1\left(f_\eta;r_{ref}\right)$, we obtain the azimuth signal in the time domain by azimuth IFFT

$$\begin{aligned}S_1\left(\eta;\eta_a,r\right)=&rect\left[\frac{\left|\eta-\eta_a\left(r-r_{ref}\right)/\left(r-r_{rot}\right)\right|}{T_1}\right]\\&\cdot\exp\left\{j\pi k_e\left(r_{ref}\right)\left(\eta-\eta_a\right)^2\right\}\end{aligned} \tag{42}$$

According to (42), time-shift occurs except for the reference range [29], which may result in time aliasing. In order to overcome this problem, the following condition should be satisfied:

$$\left|\eta_a\Delta r\right|\le\frac{\left(T_{DE}-T_1\right)\left|\left(r-r_{rot}\right)\right|}{2} \tag{43}$$

with $\Delta r=r-r_{ref}$. Then, we can further rewrite the (43) as :

$$\left|x_a x_r\right|\le\frac{v_e\left(T_{DE}-T_1\right)\left|\left(r-r_{rot}\right)\right|}{2\sin\beta} \tag{44}$$

where β is the incident angle, x_a and x_r denote the target position in azimuth and in range, respectively.

A simple simulation is performed to show the time-shift due to the range-independent deramp, using the parameters listed in Table I. Since the swath of TOPS mode is wider, the time-shift is more obvious than that in sliding spotlight mode. Therefore, we consider the TOPS mode as an example, with a 50km x 50 km (A x R) coverage. As shown in Fig. 9, the point target P_1 is located in the time aliasing area highlighted in red color, with $x_a=-25km$ and $x_r=-25km$, while the point target P_0 is located in time scene center, with $x_a=0km$ and $x_r=0km$.

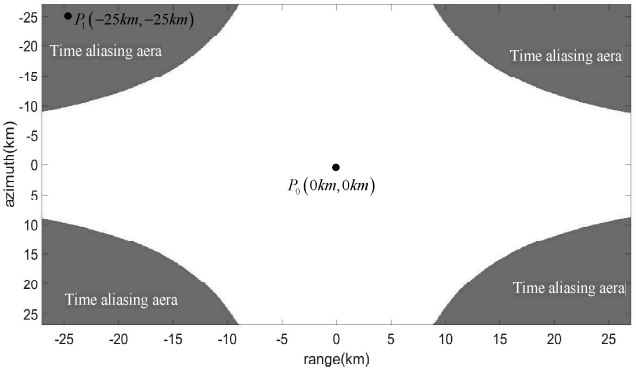

Fig. 9 Illustration of the time aliasing area highlighted in red color.

The time aliasing of P_1 is shown in Fig. 10(a), which results in the appearance of a ghost target and the pattern distortion of the impulse response function (IRF), as shown in Figs. 10(b) and 10(c) respectively. As a result, data division in range is required, by selecting different reference ranges to perform the deramp operation for each sub-data. However, this also leads to additional operations of resampling and sub-data formation, affecting the processing efficiency.

To resolve the time-shift problem, a novel method is introduced by multiplying the range-dependent deramp function, which is given by

$$H_2\left(f_\eta;r\right)=\exp\left\{j\pi\frac{f_\eta^2}{k_{rotation}}\right\}\cdot\exp\left\{-j\pi\frac{f_\eta^2}{k_e\left(r\right)}\right\} \tag{45}$$

With the range-dependent deramp operation, $S_1\left(\eta;\eta_a,r\right)$ can be rewritten as

$$S_2\left(\eta;\eta_a,r\right)=rect\left[\frac{\left|\eta\right|}{T_1}\right]\cdot\exp\left\{j\pi k_e\left(r\right)\left(\eta-\eta_a\right)^2\right\} \tag{46}$$

Then, we can compensate the residual range-dependent phase by

$$H_{residual}\left(\eta;r\right)=\exp\left\{-j\pi k_e\left(r\right)\eta^2\right\} \tag{47}$$

Thus, by the range-dependent deramp operation, the time-shift is completely removed, avoiding time aliasing and the subsequent appearance of ghost target and azimuth resolution reduction, as shown in Figs. 10(d) to 10(f).

Furthermore, azimuth weighting is applied after the range-dependent deramp operation. Since the time-shift along range dimension is removed, a simple weighting function can be applied, without moving the weighting window to accommodate the time shift. Moreover, azimuth weighting is implemented after range compression, which eliminates the energy dispersion effects due to range cell migration.

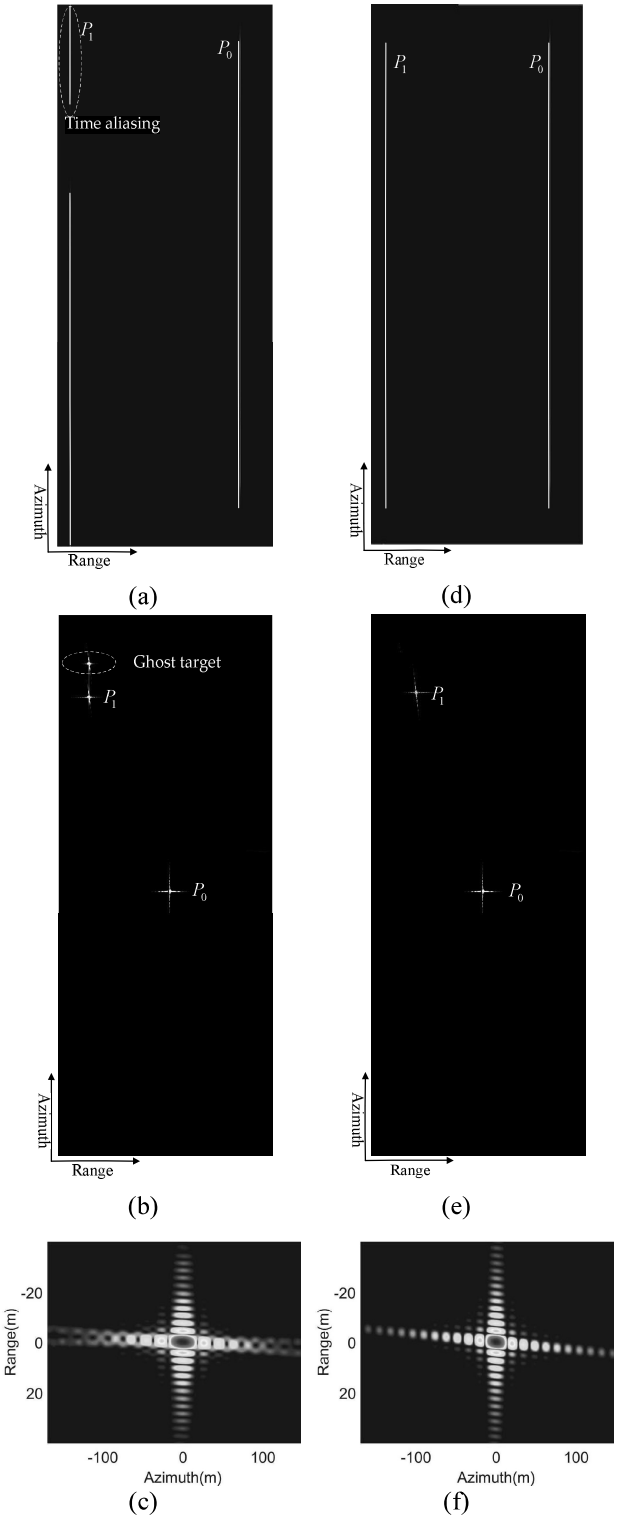

Fig. 10 Comparison of the deramp results. Using the range-independent deramp, time-shift occurs for P_1, resulting in ghost target appearance and IRF pattern distortion, as shown in (a), (b), (c). By implementing the proposed range-dependent deramp, time shift is completed removed, avoiding the ghost target and obtaining a good focusing result, as shown in (d), (e), (f).

However, if azimuth FFT is performed directly after compensation, geometry distortion will take place, due to azimuth sampling variation along the range dimension caused by range-dependent deramp. To solve this problem, CZT is adopted instead of the FFT in the final step, by selecting the range-dependent output frequency sampling interval, given by

$$\Delta f_\eta(r) = \frac{k_e(r)}{k_e(r_{ref})} \frac{f^{(1)}_{prf}}{N_A} \tag{48}$$

Therefore, the equivalent time sampling interval is:

$$\Delta\eta = \frac{k_e(r)}{\Delta f_\eta(r)} = \frac{f'_{prf}}{k_e(r_{ref}) N_A} \tag{49}$$

Since $\Delta\eta$ is range-independent, the same azimuth pixel sampling interval for all range bins is realized, which means the image geometry distortion is corrected. The detailed implementation steps are given in Fig. 6.

As shown in Fig. 11, P_1, P_2 and P_3 are located at (-25km,-25km), (0km,-25km) and (25km,-25km), respectively, having the same azimuth position but different range positions. Before geometry distortion correction, P_1, P_2 and P_3 appear at different positions in azimuth, as shown in Fig. 11(a). Using the range-dependent CZT, the geometry distortion is corrected, and P_1, P_2 and P_3 are now located at the right azimuth position.

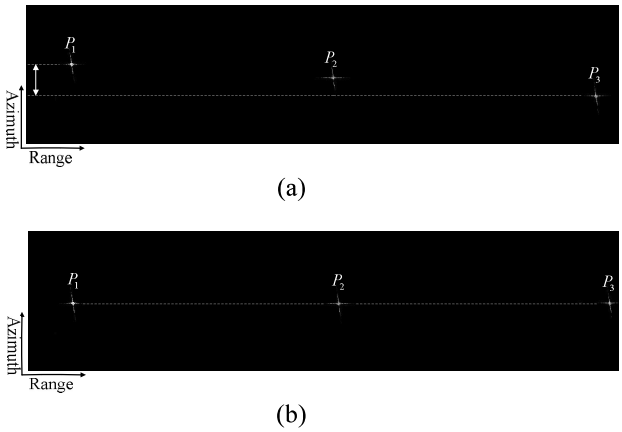

Fig. 11 Focusing results: (a) without geometry distortion correction, (b) with geometry distortion correction.

Fig. 12 gives the flowchart of the proposed three-step algorithm.

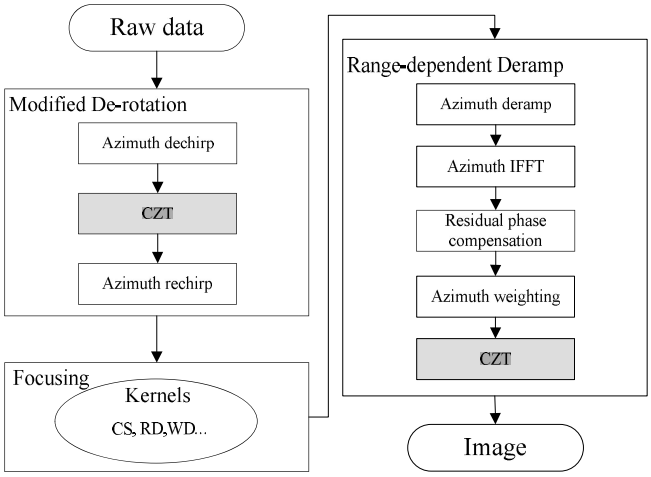

Fig. 12 Flowchart of the proposed algorithm.

IV. Experimental Results

A. Simulation Results

Imaging results on simulated raw data are employed to validate the proposed algorithm, with the parameters listed in Table I. Fig. 13 shows the 9 point targets in our simulation arranged in a scene of $50km \times 50km$ in the TOPS mode and $7km \times 7km$ in the sliding spotlight mode, respectively.

TABLE I
SIMULATION PARAMETERS

Image Parameters	TOPS	Sliding Spotlight
Wavelength	0.031 m	0.031 m
Elevation angle	30.0°	30.0°
Orbit height	600 km	600 km
Eccentricity	0.0011	0.0011
Orbit inclination angle	97°	97°
Pulse width	30 μs	30 μs
PRF	5000 Hz	4200 Hz
Signal bandwidth	50 MHz	500 MHz
Signal sampling rate	60 MHz	600 MHz
Swath coverage	50km x50 km (AxR)	7 km x7 km (AxR)

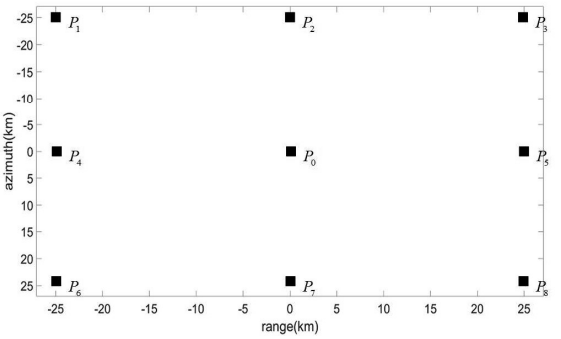

(a)

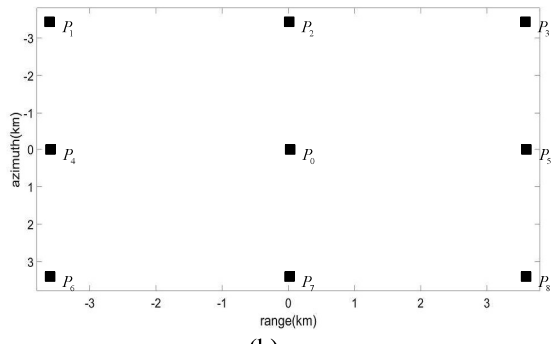

(b)

Fig. 13 Simulation scene: (a) TOPS mode, (b)sliding spotlight mode.

We use the traditional full-aperture algorithm and the proposed algorithm to process the raw data, respectively. To compare the focusing performance in the whole scene, the interpolated contour plots of the point targets P_1, P_0 and P_8 focused with the traditional and the proposed algorithms are shown in Figs. 14 and 15, corresponding to TOPS and sliding spotlight modes, respectively. Moreover, quantitative results of the imaging quality in azimuth are listed in TABLE II, including the resolution, the peak sidelobe ratio (PSLR), and the integrated sidelobe ratio (ISLR).

TABLE II
SIMULATION PARAMETERS

	Proposed algorithm			Traditional algorithm		
TOPS mode						
Point Targets	Resolution (m)	PSLR (dB)	ISLR (dB)	Resolution (m)	PSLR (dB)	ISLR (dB)
P_1	12.18	-13.27	-10.10	17.06	-12.64	-10.08
P_2	12.39	-13.25	-10.08	12.38	-13.30	-10.18
P_3	12.59	-13.26	-10.10	17.38	-13.87	-11.64
P_4	12.28	-13.28	-10.10	12.29	-13.24	-10.06
P_0	12.51	-13.26	-10.01	12.50	-13.25	-10.08
P_5	12.69	-13.26	-10.07	12.69	-13.26	-10.09
P_6	12.19	-13.26	-10.10	16.12	-13.74	-11.49
P_7	12.39	-13.25	-10.09	12.39	-13.28	-10.17
P_8	12.59	-13.26	-10.09	18.57	-12.79	-10.05
Sliding spotlight mode						
Point Targets	Resolution (m)	PSLR (dB)	ISLR (dB)	Resolution (m)	PSLR (dB)	ISLR (dB)
P_1	0.50	-13.32	-10.27	0.53	-13.24	-10.33
P_2	0.50	-13.30	-10.24	0.53	-13.26	-10.32
P_3	0.49	-13.28	-10.33	0.53	-13.24	-10.38
P_4	0.50	-13.26	-10.26	0.50	-13.26	-10.30
P_0	0.50	-13.26	-10.24	0.50	-13.26	-10.30
P_5	0.49	-13.27	-10.23	0.49	-13.27	-10.29
P_6	0.50	-13.19	-10.47	0.53	-13.32	-10.47
P_7	0.50	-13.20	-10.27	0.53	-13.27	-10.36
P_8	0.49	-13.20	-10.38	0.53	-13.20	-10.44

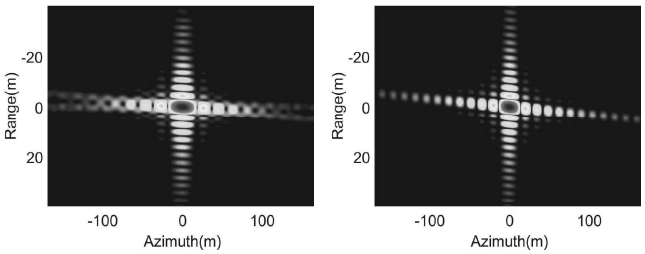

(a) (d)

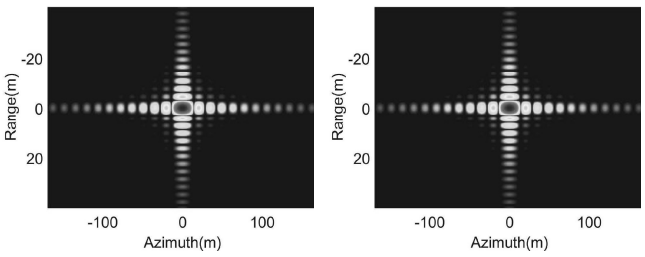

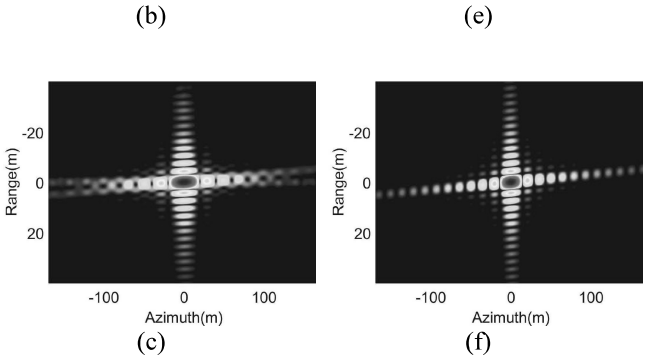

Fig. 14 TOPS data processing result. The interpolated contour plots of P_1, P_0, and P_8 focused by traditional algorithm are shown in (a)~(c) and those focused by proposed algorithm are shown in (d)~(f).

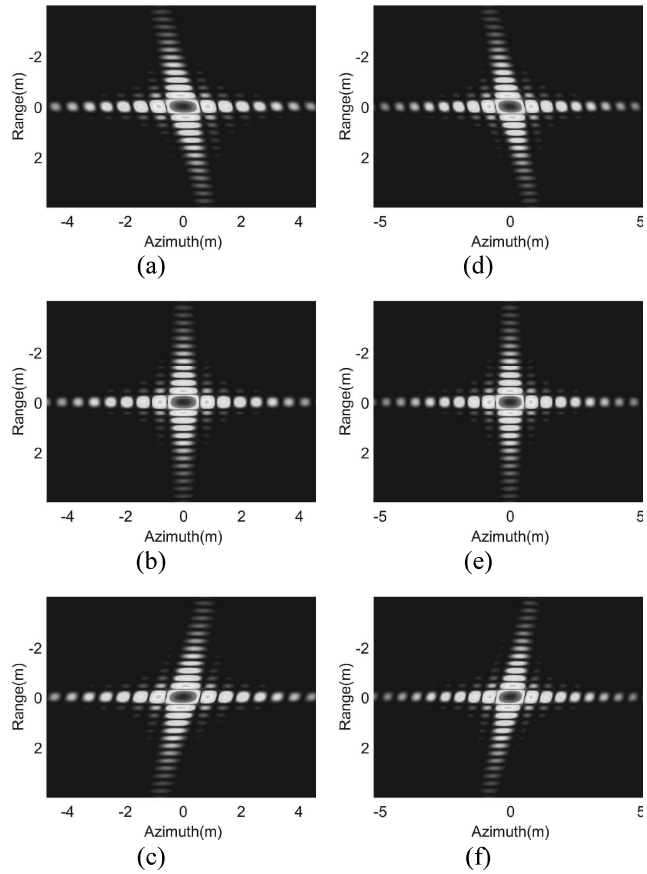

Fig. 15 Sliding spotlight data processing result. The interpolated contour plots of P_1, P_0, and P_8 focused by traditional algorithm are shown in (a)~(c) and those focused by proposed algorithm are shown in (d)~(f).

As seen from the TOPS processing results, due to time aliasing in the deramp operation, targets P_1, P_3, P_6, and P_8, located at the time aliasing area, suffer from resolution reduction and IRF pattern distortion. By implementing the proposed algorithm, time aliasing has been completely removed, leading to a good focusing performance for the whole scene. With respect to the sliding spotlight, there is no IRF pattern distortion for any target using the traditional algorithm, as shown in Fig. 15. However, since we have performed data focusing without zero-padding, there is significant Doppler spectrum aliasing, resulting in as high as 6% azimuth resolution reduction at azimuth edge, corresponding to targets P_1 - P_3 and P_6 - P_8. Using the modified de-rotation method with a scaling factor $\alpha = 0.9$, Doppler spectrum aliasing has been avoided, providing accurate focusing results for the whole scene.

B. Real Data Results

Real airborne sliding spotlight data is used here to verify the performance of the proposed algorithm. Fig. 16 shows the resultant sliding spotlight image using the modified three-step algorithm, with the main parameters listed in TABLE Ⅲ. As shown in Fig. 16, the image is well focused without image folding.

TABLE Ⅲ
Main parameters for sliding spotlight data processing

Parameters	Values
Wavelength	0.03m
Incidence angle	66°
Height	7.1km
PRF	2000Hz
Signal sampling rate	1.4GHz
Resolution	0.1m

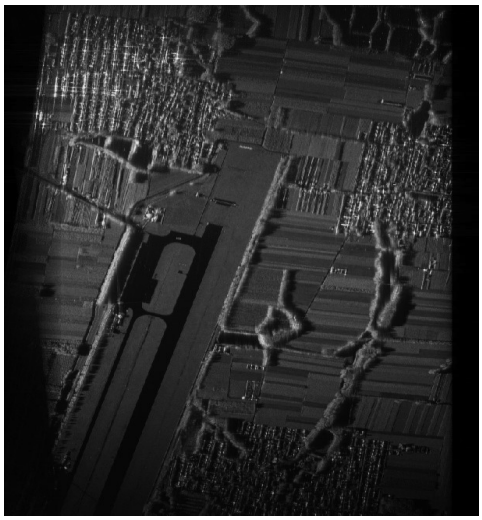

Fig. 16 Airborne sliding spotlight data processing result. The range is horizontal, and the azimuth is vertical.

V. CONCLUSIONS

In this paper, an efficient three-step algorithm has been proposed for both TOPS and sliding spotlight data processing, without zero-padding and sub-aperture formations. To overcome azimuth spectrum aliasing, a modified low-complexity de-rotation method was derived in detail using CZT instead of FFT. Moreover, to solve the azimuth folding problem in the focused image, a range-dependent deramp operation was applied. Compared with the traditional range-independent deramp operation, the proposed one can accommodate the resultant time-shift, so that data division in range is not needed any more and it is more efficient, especially in the wide-swath case. Furthermore, the CZT is adopted in the final step to replace FFT, in order to correct the image geometry distortion introduced by the range-dependent deramp operation. The

effectiveness of the proposed method was demonstrated by both simulated data and real data. Note that the proposed algorithm can also be applied for spotlight and inverse TOPS (ITOPS) data processing. As for spotlight data, it has a similar Doppler spectrum aliasing problem, which means that the CZT based de-rotation method, proposed in the first-step of the algorithm, can be adopted for avoiding spectrum aliasing. For the ITOPS data, it has both azimuth spectrum aliasing and azimuth image folding problems. Therefore, the proposed algorithm is also applicable to ITOPS data processing, by simply modifying the hybrid factor.

ACKNOWLEDGMENT

This work was supported by National Natural Science Foundation of China (NSFC) under Grant Nos. 61132006, 61171123, and 61628101.

REFERENCES

[1] F. D. Zan, A. M. Guarnieri, "TOPSAR: Terrain observation by progressive scans," *IEEE Trans. Geosci. Remote Sens.*, vol. 44, no. 9, pp. 2352-2360, Sep. 2006.

[2] A. Meta, J. Mittermayer, P. Prats, R. Scheiber, and U. Steinbrecher, "TOPS imaging with TerraSAR-X: mode design and performance analysis," *IEEE Trans. Geosci. Remote Sens.*, vol. 48, no. 2, pp. 759-769, Feb. 2010.

[3] M. Nannini, P. Prats, R. Scheiber, F. D. Zan, and D. Geudtner, "TOPS time series performance assessment with TerraSAR-X data," *IEEE J. Sel. Topics Appl. Earth Observ*, vol. 9, no. 8, pp. 3832-3848, Aug. 2016.

[4] J. Chen, H. kuang, W. Yang, W. Liu, and P. B. Wang, "A novel imaging algorithm for focusing high-resolution spaceborne SAR data in squinted sliding-spotlight mode," *IEEE Geosci. Remote Sens. Lett.*, vol. 13, no. 10, pp. 1577-1581, Oct. 2016.

[5] P. Prats, R. Scheiber, J. Mittermayer, and A. Moreira, "Processing multiple SAR modes with baseband azimuth scaling," in *Proc. IGARSS*, Cape Town, South Africa, Jul. 2009, pp. 172-175.

[6] N. Y. Martinez, P. Prats, F. R. Gonzalez, R. Brcic, R. Shau, D. Geudtner, M. Eineder, and R. Bamler, "Interferometric processing of sentinel-1 TOPS data," *IEEE Trans. Geosci. Remote Sens.*, vol. 54, no. 4, pp. 2220-2234, Apr. 2016.

[7] S. Montazeri, X. X. Zhu, M. Einder, and R. Bamler, "Three-dimensional deformation monitoring of urban infrastructure by tomographic SAR using multitrack TerraSAR-X data stacks," *IEEE Trans. Geosci. Remote Sens.*, vol. 54, no. 12, pp. 6868-6878, Dec. 2016.

[8] F. Lombardini, F. Cai, and D. Pasculli, "Spaceborne 3-D SAR tomography for analyzing garbled urban scenarios: single-look superresolution advances and experiments," *IEEE J. Sel. Topics Appl. Earth Observ*, vol. 6, no. 2, pp. 960-968, Mar. 2013.

[9] A. Moreira, P. Prati, M. Younis, G. Krieger, I. Hajnsek, and K. P. Papathanassiou, "A tutorial on synthetic aperture radar," *IEEE Geosci. Remote Sensing Mag.*, vol. 1, no. 1, pp. 6-43, Dec. 2013.

[10] S. Tebaldini, F. Rocca, A.Reigber, and L. F. Famil, "SAR tomography of natural environments: Signal processing, applications, and future challenges," in *Proc. IGARSS*, BeiJing, China, Jul. 2016, pp. 1-4.

[11] R. Scheiber, S. Wollstadt, S. Sauer, and E. Malz, "Sentinel-l imaging performance verification with TerraSAR-X," in *Proc. EUSAR,* Eurogress, Germany, Jun. 2010, pp. 55-58.

[12] J. Bello, M. Martone, T. Kraus, P. Prats, and B. Bräutigam, "Performance evaluation of TanDEM-X experimental modes," in *Proc. EUSAR,* Berlin, Germany, Jun. 2014, pp. 284-287.

[13] J. Boeer, U. Steinbrecher, M. Bachmann, D. Schulze, and B. Braeutigam, "Overview and status of TerraSAR-X/TanDem-X long term system monitoring," in *Proc. EUSAR,* Berlin, Germany, Jun. 2014, pp. 292-295.

[14] J. Janoth, S. Gantert, T. Schrage, and A. Kaptein, "TerraSAR next generation-mission capabilities," in *Proc. IGARSS*, Melbourne, Australia, Jul 2009, pp. 2297-2300.

[15] S. Gantert, A. Kern, R. During, J. Janoth, L. Petersen, and J. Herrmann, "The future of x-band SAR: TerraSAR-X next generation and WorldSAR constellation," in *Proc. APSAR,* Tsukuba, Japan, Sept. 2013, pp. 20-23.

[16] C. Prati, A. M. Guarnieri, and F. Rocca, "Spot mode SAR focusing with the $\omega-k$ technique," in *Proc. IGARSS*, Helsinki, Finland, Jun. 1991, pp. 631–634.

[17] A. M. Guarnieri, and C. Prati, "ScanSAR focusing and interferometry," *IEEE Trans. Geosci. Remote Sens.*, vol. 34, no. 4, pp. 1029-1038, Jul. 1996.

[18] W. Xu, P. P. Huang, R. Wang, Y. K. Deng, and Y. C. Lu, "TOPS-Mode raw data processing using chirp scaling algorithm," *IEEE J. Sel. Topics Appl. Earth Observ*, vol. 7, no. 1, pp. 235-245, Jan. 2014.

[19] J. Mittermayer, A. Moreira, and O. Loffeld, "Spotlight SAR data processing using the frequency scaling algorithm," *IEEE Trans. Geosci. Remote Sens.*, vol. 37, no. 5, pp. 2198-2214, Sep. 1999.

[20] P. Prati, R. Scheiber, J. Mittermayer, A. Meta, A. Moreira, and J. Sanz-Marcos, "A SAR processing algorithm for TOPS imaging mode based on extended chirp scaling," in *Proc. IGARSS*, Barcelona, Spain, Jul. 2007, pp. 148–151.

[21] P. Prati, R. Scheiber, J. Mittermayer, A. Meta, and A. Moreira, "Processing of sliding spotlight and TOPS SAR data using baseband azimuth scaling," *IEEE Trans. Geosci. Remote Sens.*, vol. 48, no. 2, pp. 770-780, Feb. 2010.

[22] W. Yang, C. S. Li, J. Chen, and P. B. Wang, "Extended three-step focusing algorithm for sliding spotlight and TOPS data image formation," in *Proc. IGARSS*, Vancouver, Canada, Jul. 2011, pp. 479–482.

[23] W. Yang, J. Chen, H. C. Zeng, J. Zhou, P. B. Wang, and C. S. Li, "A novel three-step image formation scheme for unified focusing on spaceborne SAR data," *Progr. Electromagn. Res.*, vol. 137, pp. 621–642, 2013.

[24] W. Xu, P. P. Huang, Y. K. Deng, J. T. Sun, and X. Q. Shang, "An efficient approach with scaling factor for TOPS-mode SAR data focusing," *IEEE Geosci. Remote Sens. Lett.*, vol. 8, no. 5, pp. 929-933, Sep. 2011.

[25] W. Xu, Y. K. Deng, P. P. Huang, and R. Wang, "Full-aperture SAR data focusing in the spaceborne squinted sliding-spotlight mode," *IEEE Trans. Geosci. Remote Sens.*, vol. 52, no. 8, pp. 4596-4607, Aug. 2014.

[26] J. Yang, G. C. Sun, M. D. Xing, X. G. Xia, Y, Liang, Z. Bao, "Squinted TOPS SAR imaging based on modified range migration algorithm and spectral analysis," *IEEE Geosci. Remote Sens. Lett.*, vol. 11, no. 10, pp. 1707-1711, Oct. 2014.

[27] G. Engen, and Y. Larsen, "Efficient full aperture processing of TOPS mode data," *in Proc. EUSAR,* Berlin, Germany, Jun. 2010, pp. 13-16.

[28] G. Engen, and Y. Larsen, "Efficient full aperture processing of TOPS mode data using the moving band chirp z-transform," *IEEE Trans. Geosci. Remote Sens.*, vol. 49, no. 10, pp. 3688-3693, Oct. 2011

[29] A. Moreira, J. Mittermayer, and R. Scheiber, "Extended chirp scaling algorithm for air- and spaceborne SAR data processing in stripmap and scanSAR imaging modes," *IEEE Trans. Geosci. Remote Sens.*, vol. 52, no. 8, pp. 4596-4607, Aug. 2014.

[30] A. Meta, J. Mittermayer, U. Steinbrecher, and P. Prats, "Investigations on the TOPSAR acquisition mode with TerraSAR-X," in *Proc. IGARSS*, Barcelona, Spain, Jul. 2007, pp. 152–155.

[31] A. Meta, P. Prats, U. Steinbrecher, J. Mittermayer, and R. Scheiber, "TerraSAR-X TOPSAR and scanSAR comparison," in *Proc. EUSAR,* Friedrichshafen, Germany, Jun. 2008, pp. 1-4.

[32] R. K. Raney, H. Runge, R. Bamler, I. G. Cumming, and F. H. Wong, "Precision SAR processing using chirp scaling," *IEEE Trans. Geosci. Remote* Sens., vol. 32, no. 4, pp. 786-799, Jul. 1994.

[33] I. G. Cumming, F. H. Wong, "Digital processing of synthetic aperture radar data: algorithms and implementation," Boston: Artech House; 2005.

[34] F. H. Wong, and T. S. Yeo, "New applications of nonlinear chirp scaling in SAR data processing," *IEEE Trans. Geosci. Remote Sens.*, vol. 39, no. 5, pp. 946-953, May. 2001.

[35] D. Y. Zhu, S. H. Ye, Z. D. Zhu, "Polar format algorithm using chirp scaling for spotlight SAR image formation," *IEEE Trans. Aerosp. Electron. Syst*, vol. 44, no. 4, pp. 1433-1448, Oct. 2008.

[36] R. Lanari, S. Zoffoli, E. Sansosti, G. Fornaro, and F. Serafino, "New approach for hybrid strip-map/spotlight SAR data focusing," *IEE Proc. - Radar, Sonar Naving.*, vol. 148, no. 6, pp. 363-372, Dec. 2001.

[37] R. Lanari, M. Tesauro, E. Sansosti and G. Fornaro, "Spotlight SAR data focusing based on a two-Step processing approach," *IEEE Trans. Geosci. Remote Sens.*, vol. 39, no. 9, pp. 1993-2004, Sep. 2001.

[38] L. R. Rabiner, R. W. Schafer, C. M. Rader, "The Chirp Z-Transform Algorithm," *IEEE Trans. Audio Electroacust.*, vol. AU-17, no. 2, pp. 86-92, Jun. 1969.

[39] R. Lanari, M., "A New Method for the Compensation of the SAR Range Cell Migration Based on the Chirp Z-Transform," *IEEE Trans. Geosci. Remote Sens.*, vol. 33, no. 5, pp. 1296-1299, Sep. 1995.

[40] D. Y. Zhu, and Z. D. Zhu, "Range resampling in the polar format algorithm for spotlight SAR image formation using chirp z-transform ," *IEEE Trans. Singal Process.*, vol. 55, no. 3, pp. 1011-1023, Mar. 2007

[41] P. B. Wang, W. Liu, J. Chen, and W. Yang, "A high-order Imaging algorithm for high-resolution spaceborne SAR based on a modified equivalent squint range model," *IEEE Trans. Geosci. Remote Sens.*, vol. 53, no. 3, pp. 1225-1235, Mar. 2015.

[42] Y. F. Xu, S. G. Sun, X. G. Xia, M. D. Xing, J. Yang, and Z. Bao, "An azimuth frequency non-linear chirp scaling (FNCS) algorithm for TOPS SAR imaging with high squint angle," *IEEE J. Sel. Topics Appl. Earth Observ*, vol. 7, no. 1, pp. 213-220, Jan. 2014.

[43] D. X. An, X. T. Huang, T. Jin, and Z. M. Zhou, "Extended nonlinear chirp scaling algorithm for high-resolution highly squint SAR data focusing," *IEEE Trans. Geosci. Remote Sens.*, vol. 50, no. 9, pp. 3595-3609, Sep. 2012.

[44] P. Prats, R. Scheiber, M. Rodriguez, J. Mittermayer, S. Wollstadt, and F. D. Zan, "On the processing of very high resolution spaceborne SAR data," *IEEE Trans. Geosci. Remote Sens.*, vol. 52, no. 10, pp. 6003-6016, Oct. 2014.

[45] D. Giudici, S. Mancon, A. Monti, R. Piantanida, G. Prandi, L. Recchia, and A. Recchia, " Efficient full aperture processing of TOPS mode data," *in Proc. IGARSS,* Beijing, China, July. 2016, pp. 5019-5022.